

Morphology of Binder-Jet Additive Manufactured Structural Amorphous Metal Matrix Composites

Amamchukwu B. Ilogebe, Cynthia K. Waters, Amy M. Elliot, Cameron Shackleford

^{1,2,4}North Carolina Agricultural and Technical State University

^{3,4}Oak Ridge National Laboratory

Corresponding Author: Amamchukwu B. Ilogebe

ABSTRACT

Binder-jet 3D printing is one of the additive manufacturing (AM) techniques employed in the fabrication of intricate parts, by utilizing metal powders. Many implementations of AM exist from areas as diverse as the food industry to biomedical engineering; such a broad-spectrum usage of this technology makes it extremely attractive when combined with its low cost, reliability, color range, and complexity abilities. [1]. In this work, a method of making metal matrix composite was adopted which involves printing metal samples from gas atomized powder and infiltrating a lower melting metal into the porous sites of the sample. To achieve this, gas atomized structural amorphous metal (SAM) alloy powder was used for Binder-jet 3D printing of the base samples, while Bronze pellets were utilized for unpressurized liquid metal infiltration because of its lower melting temperature and high ductility. The SAM alloy powder was first characterized by Morphologi G3. The samples obtained were characterized by scanning electron microscopy, electron dispersive x-ray as well as micro-indentation. Liquid metal infiltration of bronze into binder-jet printed structural amorphous metal resulted in fully-dense net-shape parts. Electron dispersive spectroscopy results show that the bronze filled out the pores as expected. Micro-indentation results show a variation of hardness across the metal matrix as the SAM alloy sections exhibit higher hardness than the bronze sections. Generally, it was found that the infiltration of bronze into structural amorphous metal improved the homogeneity of the material and makes the samples denser.

KEYWORDS; -Amorphous Metal, Binder-jet printing, Infiltration, Porosity, Density

DATE OF SUBMISSION: 30-06-2019

DATE OF ACCEPTANCE: 19-07-2019

I. INTRODUCTION

Over the last few decades, there has been enormous research on Fe-based amorphous and nanocrystalline alloys with high amorphous-forming ability and good properties. This has called for research on applications in sports equipment, surgical tools, military, coating industries, etc., due to its excellent mechanical properties, high corrosion and wear resistance, low young modulus, high hardness strength, high stiffness, high elastic modulus and low cores loss, and even high magnetic permeability [2][3][4][5]. In their research, the Defense Advanced Research Project Agency (DARPA) described it unique, compelling and enabling application in several Department of Defense (DOD) areas (e.g., ship hulls, aircraft structures, penetrators, etc.), DARPA plans to develop the science and technology of this field, and demonstrate its utility in challenging problems. Structural amorphous metals (SAM), also referred to as bulk metallic glasses (BMG), are produced by rapid quenching (RQ) or mechanical alloying (MA). The latter is found to be easier, more versatile and more convenient technique [6]. The rapid quenching process requires ultra-fast solidification from the liquid state. This can be achieved through different casting techniques: low-pressure copper mold casting, arc-melt casting, high pressure die casting, centrifugal casting, suction castings, and squeeze casting. Mechanical alloying (MA) is the process by which a mixture of pre-alloy powders is ball-milled, creating mechanically activated powders [5].

The production of parts through metal powder compaction has been tremendous, as it reduces post-processing, such as machining, which poses a major problem due to the high hardness of these materials. To avoid potentially post-processing, binder-jet 3D printing can be employed in the production of intricate parts. Research has shown that parts printed from binder-jet printing possess low densification, which in this research was checked by pressureless liquid metal infiltration. In binder-jet 3D printing, powders are held together by the organic binders as the part is built up layer-by-layer. conversely, liquid metal infiltration is a fabrication technique in which a preformed dispersed phase is soaked in a molten metal matrix, which fills the pores between the dispersed phase inclusions. The pressureless infiltration process involves infusion of molten liquid

metal into the pores of the porous body without applying external pressure [7][8][9][10]. According to Choi et al, if pressure-less infiltration is carried out in a controlled temperature and gas atmosphere, and good wetting condition, good infiltration can be accomplished [11]. Some of the advantages of this production technique are less time consuming and minimal post processing needed.

II. EXPERIMENTAL METHOD

A 200kg of rapidly solidified SAM alloy powder was obtained from Oak Ridge National Laboratory. The first step was to characterize the powder. The composition of the powder received is given in Table 1 and the powder morphology in Figure 1. The morphology of the rapidly-solidified powder is irregular in shape with different particle sizes. This alloy was designed so that when it is heated, thermally-stable carbides and borides precipitate and prevent grain growth [12]. The SAM alloy powder was sieved to remove particles larger than 45µm which can interfere with printing and or cause large pores in the samples.

Table 1: Composition in wt. % of SAM alloy powder

Fe	Cr	Mo	V	B	C	Si	O
49	18.6	15.8	8.9	3.4	3.3	1.08	0.02

High purity commercial Bronze powder of -325mesh was purchased from Metal Powder USA, Temecula California. The powder was used for Liquid Metal Infiltration (LMI). Bronze was chosen because, at higher saturation, incremental pore-filling is dictated by local pore geometrical characteristics, and saturation curves obeying then the Brooks-Corey correlation [13][14][15]. The saturation corresponding to non-wetting fluid is given by:

$$S = \frac{V_m}{1 - V_r} \quad 1$$

Where V_m and V_r are volume fraction of base metal and the reinforcement metal respectively.

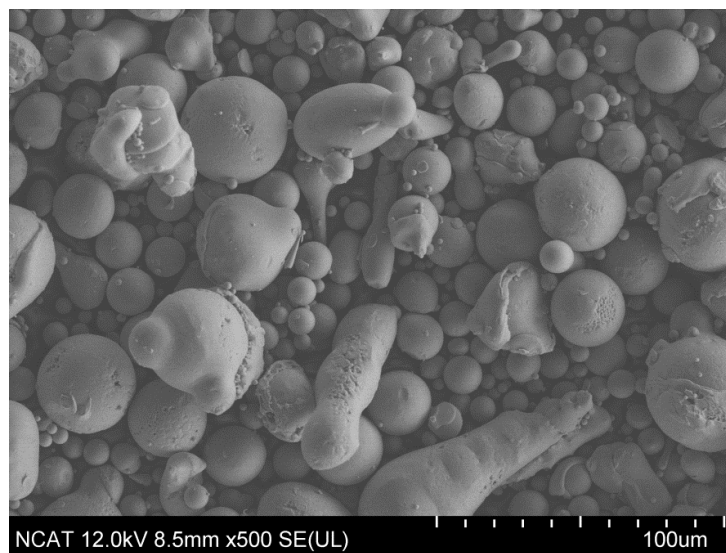


Figure 1:Morphology of SAM alloy3 powder

Morphological Characterization

Automated imaging is a way to study the morphological characteristics of particulate materials. The combination of size and shape data can be used to classify particles as agglomerates, as suggested by Malvern’s new guidance, enabling the amount of agglomerated material present in the blend to be quantified. With this tool, circularity, volume, and number distribution, as well as convexity, could be important in determining the morphology (size and shape) of powder particles being used [16].

Morphologi G3 was used to analyze powder particle shapes and sizes. The Morphologi G3-ID extends the capabilities of image analysis by applying the technique of morphologically directed Raman spectroscopy to enable the chemical identification of multi-component agglomerates that cannot be reliably classified based on size and shape alone [17].

Binder-Jet Printing

The samples were printed from the gas atomized powder using an ExOne Lab 3D printer. The entire powder bed was heated to 200°C for two hours; the binder was cured and the green parts were then de-powdered. The printed samples were sintered and infiltrated. The sintering was carried out according to the heating schedule shown in Figure 2. This schedule was based on the one that was developed for 420 stainless steel powders [18]. The temperature was held at 600 °C is to burn-out the binder.

Samples for Scanning Electron Microscopy (SEM) characterization were prepared using standard metallographic techniques. The samples were mounted in resin, cross-sectioned, ground, polished and etched. Hitachi SU8000 equipped with an energy dispersive spectroscopy (EDS) detector was used for SEM imaging and EDS analysis.

Micro Hardness Test

The Vickers microhardness test was also carried out using LECO M-400-H1 micro-hardness testing equipment with 15s hold time. The test was carried out according to ASTM Standard E384-11 to investigate the hardness of sintered SAM alloy3 samples as well as the infiltrated samples. Indents were made across the cross-sections. Micro-indentation tests were conducted using the indentation force of 500 and 1000gf for thirty seconds, ensuring a distance of at least 2.5 Vickers diagonal as specified by the ASTM standard. Vickers hardness is calculated using equation 2 [19];

$$HV = \frac{1854.4P}{d^2} \quad 2$$

Where P is the applied force and d is the average Vickers diagonal; (1HV = 9.807MPa = 0.009807GPa)

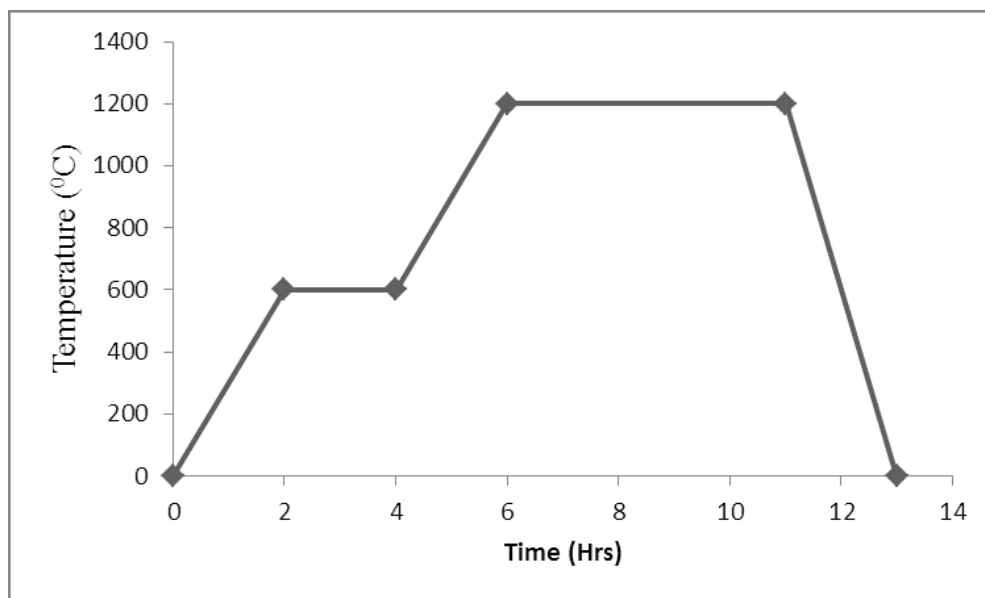


Figure 2: Heating profile for sintering

III. RESULT AND DISCUSSION

Morphologi G3 Analysis

The morphological analysis results are presented in figures 3a, b, c & d. These results were obtained from over 230,000 particles counted by morphologi G3 equipment. In figure 3(a), the average High Sensitive (HS) Circularity was 91.3 percent. This indicates that most of the SAM alloys powder particles are circular; however, the bigger particles as seen in Figure 1 are less circular. Similarly, the average aspect ratio (the proportional relationship between the particles' width and length) as shown in figure 3(b) is 0.881, which shows how circular the particles are. Figures 3(c) & (d) present the Capillary Electrophoresis (CE) diameters for volume and number distributions respectively. The minimum and maximum CE diameters were 0.54µm and 340.54µm respectively for both volume and number distribution. The difference in particle sizes was evident from the CE diameter analysis, as the standard deviations for volume and number distributions were 8.79µm and 8.08µm respectively. Information about the morphology and size distribution of SAM alloy3 powder used were seen from the Morphologi G3 data obtained.

HS Circularity - Number Distribution

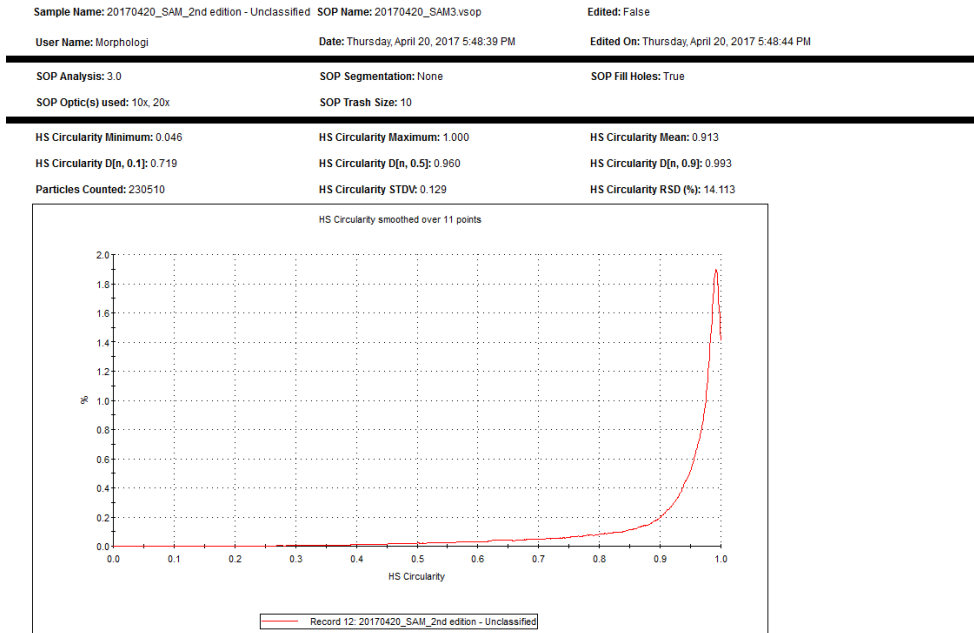


Figure 3a: Morphological Analysis showing HS Circularity – Number distribution

Aspect Ratio - Number Distribution

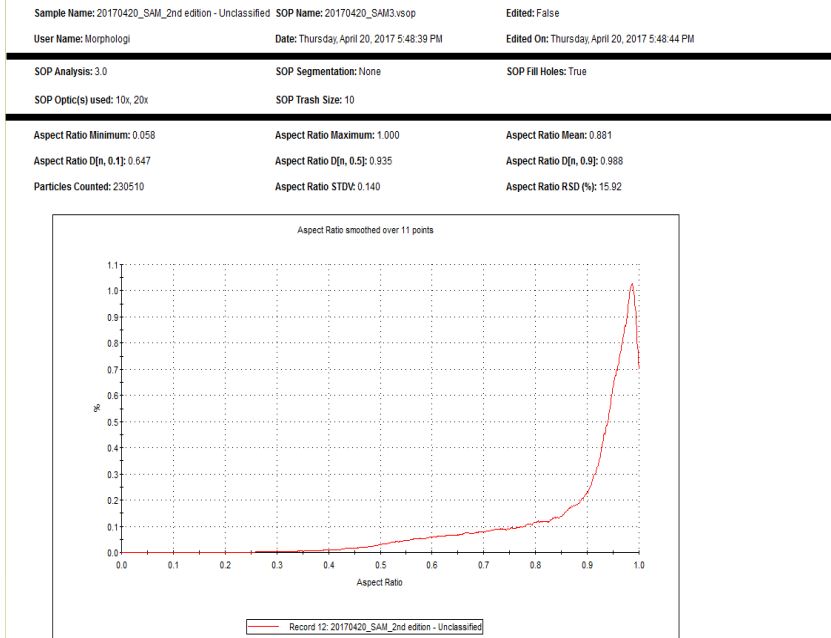


Figure 3b: Morphological Analysis showing Aspect ratio – Number distribution

CE Diameter - Volume Distribution

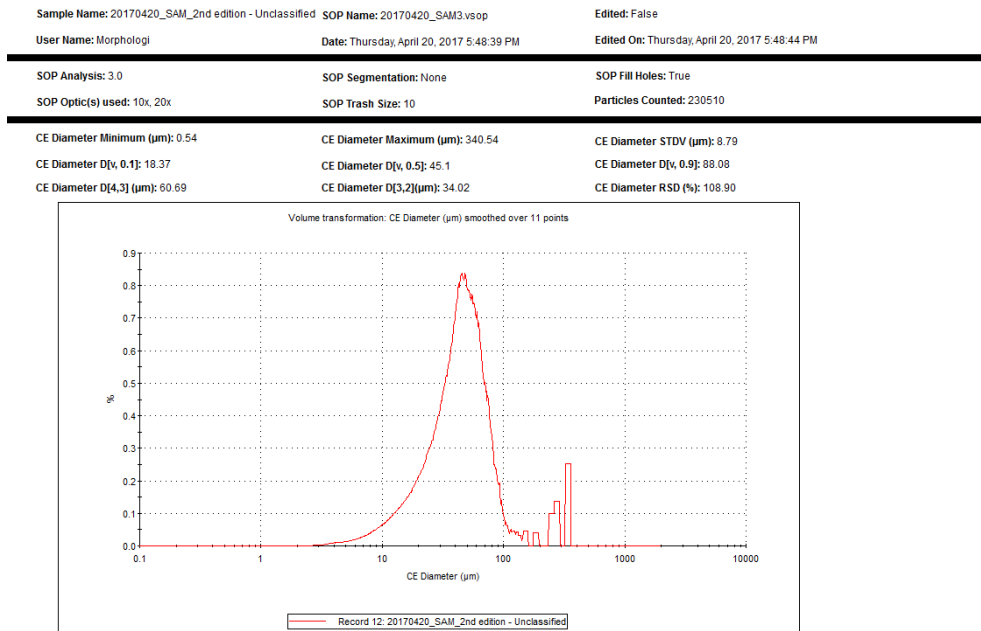
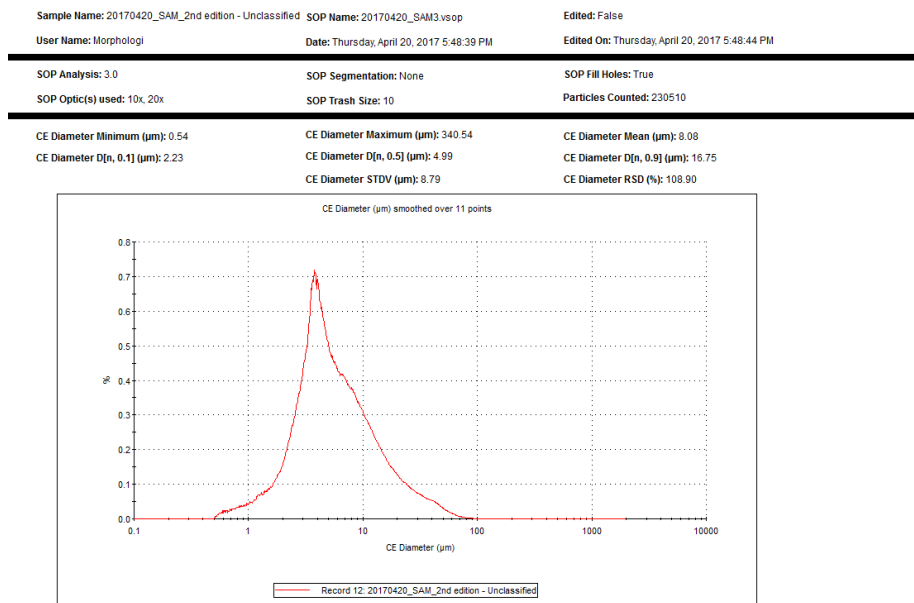


Figure 3c: Morphological Analysis, showing CE Diameter - Volume distribution

CE Diameter - Number Distribution



Comments:

Figure 3d: Morphological Analysis showing CE Diameter – Number distribution

Scanning Electron Microscopy

Figures 4, 5 and 6 are scanning electron microscope (SEM) images of sintered and liquid metal (bronze) infiltrated parts. Figures 4(a) and 4(b) clearly show SAM alloy particles forming a sintered neck with each other. This is clear evidence that diffusion occurred in the samples. Diffusion is one of the principal agents/mechanisms of sintering. Figures 5(a) and 5(b) show cross-sectional images of sintered samples of SAM alloy3 obtained at 500µm and 2000µm magnifications respectively after they were mounted on resin, polished and etched. From these figures, the dark-colored regions in between the particles are the macroporous sites, filled by the resin used for mounting the samples, while the light color regions are the SAM alloy part.

Micropores were also evident inside the SAM alloy particles, which are inherent from the as-received powder. These micropores were not filled by the infiltrant as they exist in the interior of the powder particles. Figures 6(a) and 6(b) show cross-sectional SEM images of SAM alloy infiltrated with bronze, at 500 μm and 2000 μm magnification respectively. These images show a near-perfect part as the microporous sites were filled by bronze. The bronze infiltrant formed a cobweb-like part around the SAM alloy particles. Thus, apart from the preexisting micropores in the SAM interior, every other pore created from the binder jet printing appears to be filled.

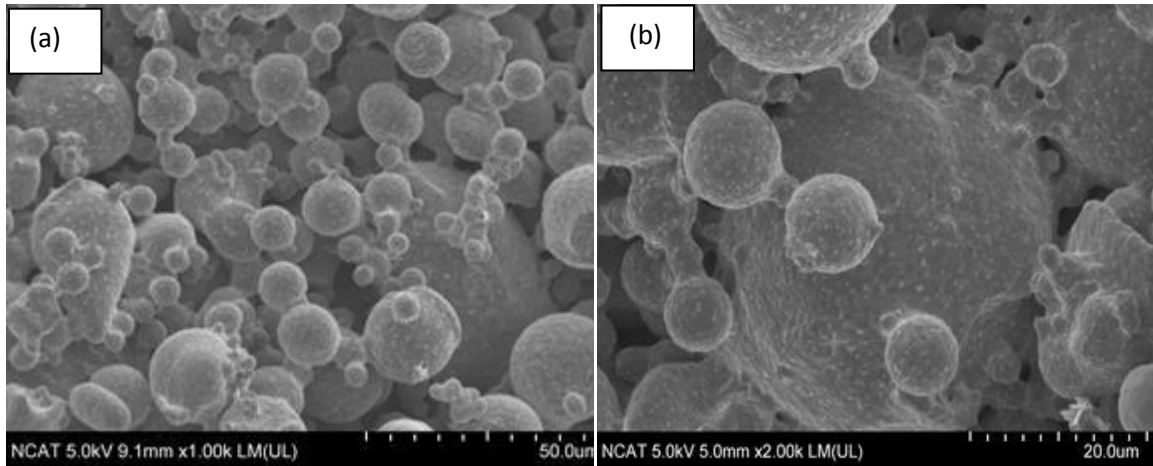


Figure 3: SEM images (a) sintered sample X500. (b) Sintered sample X2k

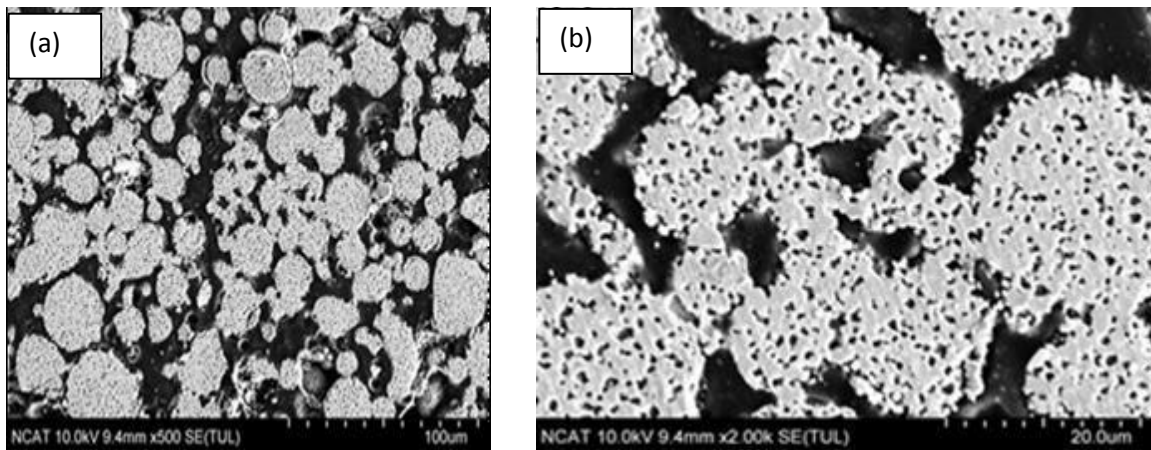


Figure 4: SEM images (a) polished sintered sample X500. (b) Polished sintered sample X2k

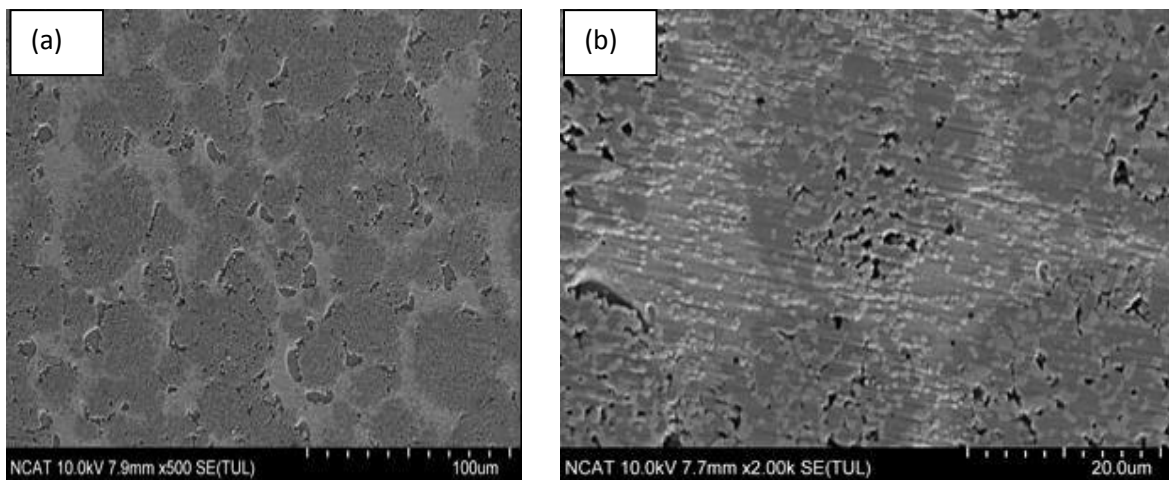


Figure 5: SEM images (a) polished Infiltrated sample X500 (b) polished Infiltrated sample X2k

Electron Dispersive X-Ray

Energy dispersed x-ray spectroscopy (EDS) was used to study the elemental distribution in the samples. EDS analysis of several samples was done using hyper mapping to determine the distribution and quantities of Fe, Mo, Cr, C, and other elements present in the samples. These elements were selected because they are either a major component of SAM3 or common by-products of the process. The hyper mapping in Figure 7(a-d) clearly shows the distribution of these elements. Carbon (Figure 7b red) was highly seen around the porous regions, which was filled with high-rich carbon quick-mount resin. Other elements are evenly distributed in the sample material regions; compare to the image in figure 7(a), as expected.

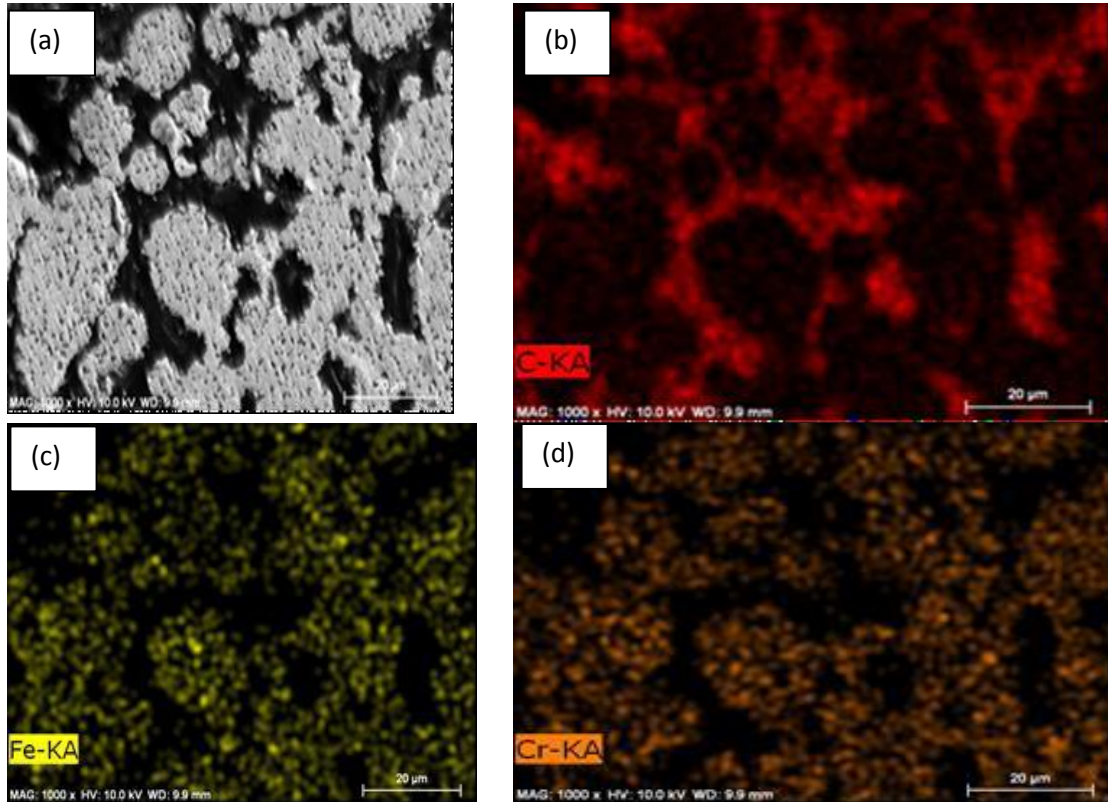


Figure 6: Hyper mapping of SAM alloy3 sample. (a) Sintered sample, (b) Carbon, (c) Iron, and (d) Chromium

The quantitative analysis of the elements, as obtained from the mapping is giving in Table 2. From the data obtained from spectrum acquisition, the high percentage of carbon recorded was as a result of the high-rich carbon quick-mount resin which occupied the porous sites, as well as the carbon composition in the SAM alloy3.

Hyper mapping analysis was also used to analyze the bronze infiltrated samples. Figures 8(a-d) present the result obtained from the hyper mapping of the infiltrated samples, while quantitative analysis of the elements present in the infiltrated sample, as obtained from the mapping, is giving in Table 3. Similarly, the elemental distribution obtained from the infiltrated samples has the same pattern as in the sintered samples, with the inclusion of copper and tin, which both make up the bronze infiltrate. Copper (and tin) assumed the position of carbon as can be seen in Figures 8(b). Thus, it filled up the porous regions. Iron, chromium, and other elements present were evenly distributed across the SAM alloy3 regions.

Table 2: Spectrum composition analysis of SAM alloy3

EL	AN	Series	Unn.(wt.%)	C norm (wt.%)	C Atom (at.%)	Error (wt.%)
C	6	K-series	57.77	65.33	78.59	7.6
O	8	K-series	6.20	7.45	4.56	33.0
Fe	26	K-series	21.00	22.31	15.93	0.9
Mo	42	L-series	1.47	1.66	0.25	0.1
Cr	24	K-series	1.34	1.52	0.42	0.2
V	23	K-series	0.48	0.55	0.16	0.1
Si	14	K-series	0.17	0.19	0.10	0.0
B	5	K-series	0.00	0.00	0.00	0.0
Total			88.43	100.00	100.00	

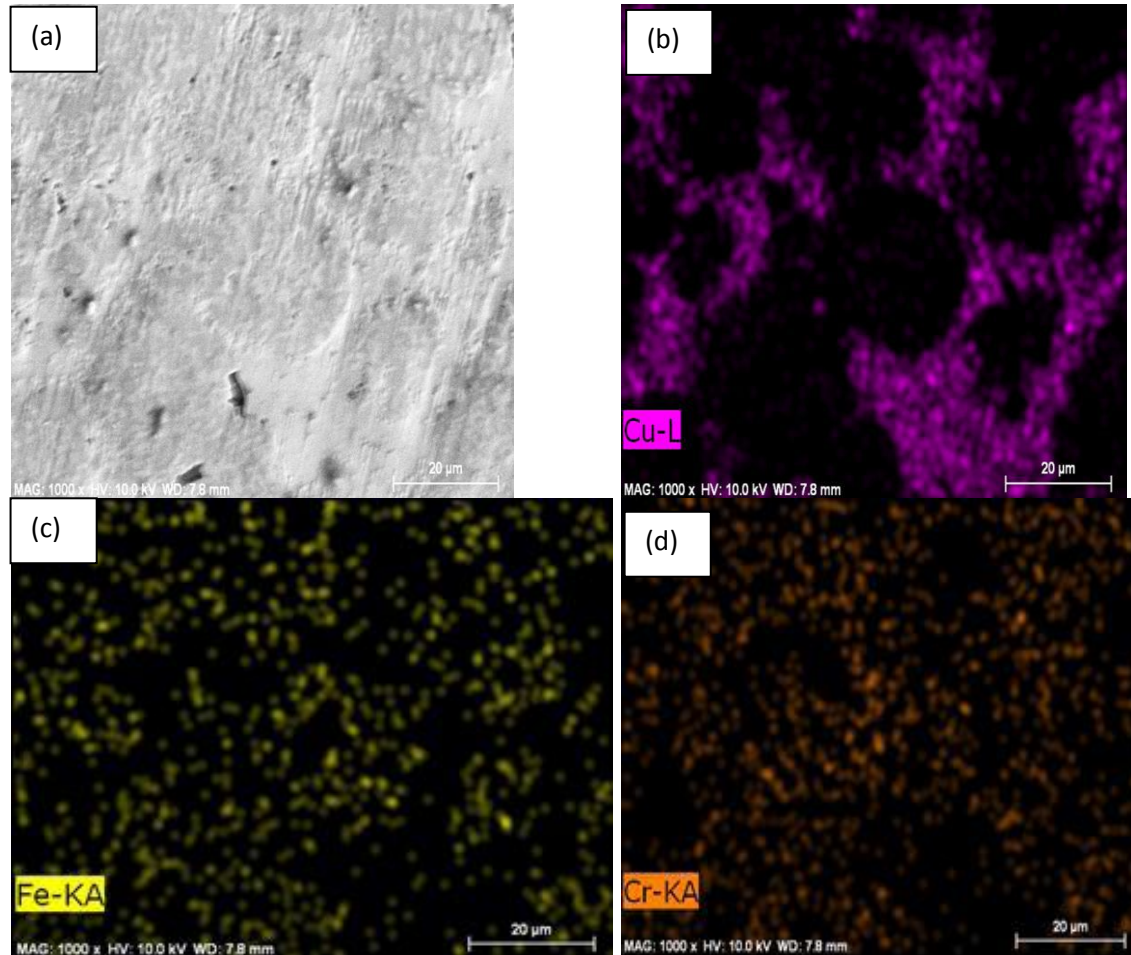


Figure 7: Hyper mapping of infiltrated SAM alloy3 sample. (a) Infiltrated sample, (b) Copper, (c) Iron, and (d) Chromium

Table 3: Spectrum composition analysis of SAM alloy3 infiltrated with bronze

EL	AN	Series	Unn.(wt.%)	C norm (wt.%)	C Atom (at.%)	Error (wt.%)
Cr	24	K-series	9.35	11.91	10.97	1.3
Fe	26	K-series	21.26	28.35	29.23	1.4
C	6	K-series	11.26	10.37	16.40	2.9
V	23	K-series	8.36	7.61	6.35	0.6
Mo	42	L-series	7.53	9.56	8.18	0.4
O	8	K-series	1.59	2.73	4.03	0.6
Cu	29	L-series	19.68	26.86	22.43	0.4
Si	14	K-series	2.01	0.71	1.01	0.0
Sn	50	L-series	1.59	1.90	1.40	0.0
Total			82.63	100.00	100.00	

Micro Indentation

The Vickers micro-hardness test of the sintered and infiltrated SAM alloy3 samples were taken in three regions of the samples, SAM alloy3 region, Bronze region, and the boundary region, referred to in this research as SAM alloy-Bronze part. The Vickers hardness results show that there is relative hardness across different regions of the infiltrated part. The results show that the SAM alloy part has an average of 936 HV 100gf, while the SAM alloy-Bronze boundary area has an average of 550 HV 100gf and the Bronze part with an average of 370 HV 100gf. Alternatively, the Vickers hardness results were 9MPa, 5MPa, and 4MPa for SAM alloy, SAM-Bronze, and Bronze parts respectively, when a 100 gram-force was applied. Figure 9 shows the relative trend of the hardness test after 16 indents were made in each of the regions.

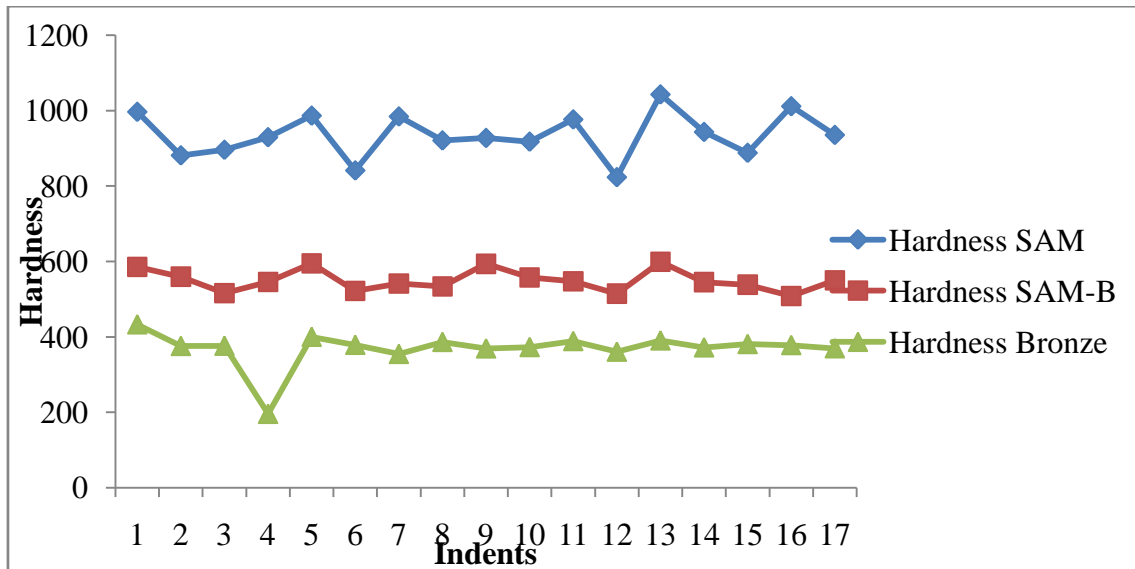


Figure 8: Micro Indentation result

IV. CONCLUSION

The development of binder-jet printed parts from SAM alloy3 power and liquid metal infiltration part with bronze was a success. Homogeneity was achieved through liquid metal infiltration, while hardness was determined. From the analysis and characterization done, the following conclusions were drawn:

- From morphology analysis, SAM alloy powder particles used was 91.3 percent circular considering over 230,000 particles analyzed. Similarly, the average aspect ratio, which is the proportional relationship between the particles' width and length was 0.881; this in other words is a measure of circularity of the particles.
- The wide range of particle sizes of the SAM alloy powder is enormous, with standard deviation of 8.08 μ m and 8.78 μ m for number and volume distribution respectively.
- The reinforcement material completely melted into the SAM alloy porous sites (sample thickness 1.10mm). A thicker geometry part may experience only partial infiltration.
- There equally exist micropores in the interiors of the powder particles, presumably resulted during gas atomization. These micropores were not filled during infiltration, because they were enclosed by the outer shell of the powder particles.
- The infiltration resulted in metal matrix composites, as both materials tend to retain their original properties as seen in the micro-indentation result.

REFERENCE

- [1]. Fidan I., Elliott A., Cossette M., Singer T., Tackett E. (2018) The Development and Implementation of Instruction and Remote Access Components of Additive Manufacturing. In: Auer M., Azad A., Edwards A., de Jong T. (eds) *Cyber-Physical Laboratories in Engineering and Science Education*. Springer, Cham. https://doi.org/10.1007/978-3-319-76935-6_13
- [2]. Han, Y., Kong, F. L., Han, F. F., Inoue, A., Zhu, S. L., Shalaan, E., & Al-Marzouki, F. (2016). New Fe-based soft magnetic amorphous alloys with high saturation magnetization and good corrosion resistance for dust core application. *Intermetallics*, 76, 18-25. doi:<http://dx.doi.org/10.1016/j.intermet.2016.05.011>
- [3]. Inoue, A., Kong, F. L., Man, Q. K., Shen, B. L., Li, R. W., & Al-Marzouki, F. (2014). Development and applications of Fe- and Co-based bulk glassy alloys and their prospects. *Journal of Alloys and Compounds*, 615, Supplement 1, S2-S8. doi:<http://dx.doi.org/10.1016/j.jallcom.2013.11.122>
- [4]. Jiles, D. C. (2003). Recent advances and future directions in magnetic materials. *Acta Materialia*, 51(19), 5907-5939. doi:<http://dx.doi.org/10.1016/j.actamat.2003.08.011>
- [5]. Neamtu, B. V., Chicinaş, H. F., Marinca, T. F., Isnard, O., Chicinaş, I., & Popa, F. (2016). Synthesis of amorphous Fe₇₅Si₂₀-xMxB₅ (M = Ti, Ta, Zr) via wet mechanical alloying and its structural, thermal and magnetic characterisation. *Advanced Powder Technology*, 27(2), 461-470. doi:<http://dx.doi.org/10.1016/j.apt.2016.01.027>
- [6]. de Oliveira, M. F., Almyras, G. A., & Evangelakis, G. A. (2015). Structural differences of amorphous Cu₆₅Zr₃₅ between rapidly quenched and topologically destabilized crystalline Cu and Zr metals by molecular dynamics simulations. *Computational Materials Science*, 104, 92-97. doi:<http://dx.doi.org/10.1016/j.commat.2015.03.041>
- [7]. Kelly, A., & Zweben, C. H. (2000). *Comprehensive composite materials*: Elsevier.
- [8]. Reid, S. R., & Zhou, G. (2000). *Impact behaviour of fibre-reinforced composite materials and structures*: Elsevier.
- [9]. Sree Manu, K. M., Ajay Raag, L., Rajan, T. P. D., Gupta, M., & Pai, B. C. (2016). Liquid Metal Infiltration Processing of Metallic Composites: A Critical Review. *Metallurgical and Materials Transactions B*, 47(5), 2799-2819. doi:10.1007/s11663-016-0751-5
- [10]. Zahedi, A., Javadpour, J., Rezaie, H., & Mazaheri, M. (2011). The effect of processing conditions on the microstructure and impact behavior of melt infiltrated Al/SiCp composites. *Ceramics International*, 37(8), 3335-3341.

- [11]. Choi, B. J., Chen, A. B., Yang, X., & Chen, I. W. (2011). Purely Electronic Switching with High Uniformity, Resistance Tunability, and Good Retention in Pt-Dispersed SiO₂ Thin Films for ReRAM. *Advanced Materials*, 23(33), 3847-3852.
- [12]. Cordero, Z., & Elliott, A. (2016). collaboration for the advancement of indirect 3d printing technology.
- [13]. Gostick, J. T., Fowler, M. W., Ioannidis, M. A., Pritzker, M. D., Volfkovich, Y. M., & Sakars, A. (2006). Capillary pressure and hydrophilic porosity in gas diffusion layers for polymer electrolyte fuel cells. *Journal of Power Sources*, 156(2), 375-387.
- [14]. Kewen, L. (2004). Theoretical development of the Brooks-Corey capillary pressure model from fractal modeling of porous media. Paper presented at the SPE/DOE Symposium on Improved Oil Recovery.
- [15]. Léger, A., Weber, L., & Mortensen, A. (2014). Infiltration of tin bronze into alumina particle beds: influence of alloy chemistry on drainage curves. *Journal of Materials Science*, 49(22), 7669-7678. doi:10.1007/s10853-014-8475-x
- [16]. Shyamal C. Das, Srinivas Ravindra BabuBehara, David A.V. Morton, Ian Larson, Peter J. Stewart,(2013). Importance of particle size and shape on the tensile strength distribution and de-agglomeration of cohesive powders, In *Powder Technology*, Volume 249, Pages 297-303, ISSN 0032-5910, <https://doi.org/10.1016/j.powtec.2013.08.034>.
- [17]. Campaña, A. Benito-Calvo, A. Pérez-González, J.M. Bermúdez de Castro, E. Carbonell, (2016). Assessing automated image analysis of sand grain shape to identify sedimentary facies, Gran Dolina archaeological site (Burgos, Spain), In *Sedimentary Geology*, Volume 346, Pages 72-83, ISSN 0037-0738, <https://doi.org/10.1016/j.sedgeo.2016.09.010>.
- [18]. Sun L, Kim Y, Kim D, Kwon P. Densification and Properties of 420 Stainless Steel Produced by Three-Dimensional Printing With Addition of Si₃N₄ Powder. *ASME. J. Manuf. Sci. Eng.* 2009;131(6):061001-061001-7. doi:10.1115/1.4000335.
- [19]. McGhee, P.,Wear Behavior Characterization for the Screening of Magnesium-Based Alloys, in*Mechanical Engineering*. 2014, North Carolina Agricultural and Technical State University: Pro-Quest. p. 1-106

Amamchukwu B. Ilogebe" Morphology of Binder-Jet Additive Manufactured Structural Amorphous Metal Matrix Composites" *The International Journal of Engineering and Science (IJES)*, 8.7 (2019): 15-24